geosciences

MDPI

Article

Formation of Gold Alloys during Crustal Differentiation of Convergent Zone Magmas: Constraints from an AU-Rich Websterite in the Stanovoy Suture Zone (Russian Far East)

Nikolai Berdnikov [1,*], Pavel Kepezhinskas [1,*], Natalia Konovalova [1] and Nikita Kepezhinskas [2]

[1] Kosygin Institute of Tectonics and Geophysics, Russian Academy of Sciences, 680000 Khabarovsk, Russia; turtle_83@mail.ru

[2] Department of Earth and Atmospheric Sciences, University of Alberta, Edmonton, AB T6G 2R3, Canada; kepezhin@ualberta.ca

* Correspondence: nick@itig.as.khb.ru (N.B.); pavel_k7@yahoo.com (P.K.)

Abstract: Gold is typically transported by mafic and evolved magmas into the upper crust to be deposited in shallow oxidized porphyry and epithermal environments. However, the magmatic behavior of gold is still poorly understood and warrants further attention. Additional insights into the magmatic evolution of gold and other noble metals can be provided by investigations of primitive convergent zone magmas and products of their differentiation that contain primary-textured Au-alloys. One of the best examples of such Au-rich ultramafic cumulates is the Triassic (232–233 Ma) Ildeus intrusion, which was emplaced within the Mesozoic Stanovoy subduction zone in the Russian Far East. Some websterites from the Ildeus intrusion, representing cumulates crystallized from a primitive convergent zone magma, are enriched in Au (up to 596 ppm) and contain abundant Cu-Ag-Au micro-particles. Most of these Au-alloy micro-particles display compositions similar to those previously found in explosive pyroclastic rocks in the Lesser Khingan iron district, mantle wedge peridotites in Kamchatka and Cretaceous adakites in the Stanovoy suture zone. Textural and compositional characteristics suggest that Cu-Ag-Au alloys precipitated from a primitive calc-alkaline melt during its crustal differentiation in a Mesozoic paleo-subduction zone. Some large Cu-Ag-Au grains display an internal honeycomb-like structure with alternating Cu-rich and Cu-poor zones. Heating experiments under atmospheric conditions recorded a substantial loss of Cu from primary magmatic Cu-Ag-Au alloys, which appears to be a process characteristic of oxidized hydrothermal ore systems. We suggest that the later-stage hydrothermal alteration of differentiated igneous conduits containing magmatic gold alloys results in the formation of Cu-free gold mineralization comparable to the upper crustal porphyry and epithermal environments.

Keywords: Stanovoy subduction zone; Ildeus intrusion; ultramafic cumulates; convergent zone magmas; primary-magmatic gold; Cu-Ag-Au alloys; Cu removal; hydrothermal fluids; mesothermal-epithermal native Au

Citation: Berdnikov, N.; Kepezhinskas, P.; Konovalova, N.; Kepezhinskas, N. Formation of Gold Alloys during Crustal Differentiation of Convergent Zone Magmas: Constraints from an AU-Rich Websterite in the Stanovoy Suture Zone (Russian Far East). *Geosciences* **2022**, *12*, 126. https://doi.org/10.3390/geosciences12030126

Academic Editors: Maurizio Barbieri and Jesus Martinez-Frias

Received: 27 January 2022
Accepted: 28 February 2022
Published: 8 March 2022

1. Introduction

Gold is an important commercial metal in various types (porphyry, epithermal, volcanogenic massive sulfide, Carlin-type, intrusion-related, etc.) of ore deposits at convergent plate margins [1–12]. Because of their high solubility in a wide range of silicate melts and hydrothermal fluids, gold and associated base and precious metals (Ag, Cu, Mo, Pt, Pd) are transported into the upper crust by metal-rich, basaltic to dacitic magmas and deposited in epithermal and porphyry environments in subduction and collision zones [3–6,11,13–20]. The post-magmatic evolution of various gold mineral species in these shallow oxidized settings has been relatively well documented. Gold is primarily included in sulfides or forms tellurides, bismuthides and sulfosalt minerals in porphyry and epithermal ores [21–27]. On the contrary, magmatic behavior of Au during crustal differentiation of magmas is

still quite poorly understood [18,28,29]. Therefore, well-characterized mineralized plutonic complexes in ancient subduction settings, representing cumulates of primary arc magmas [30–32]) are capable of providing critical insights into the magmatic behavior of gold in crustal environments. The principal aim of this paper, therefore, is to shed some additional light on this issue by looking at a unique sequence of cumulate intrusive rocks carrying primary magmatic Au-bearing alloys. Gold mineralization in subduction-related plutonic environments is traditionally linked to intermediate and felsic magmas and associated hydrothermal fluids [1,3,11,33–35]. Arc-related ultramafic-mafic plutonic complexes frequently carry base metal sulfide mineralization, for which gold might be a minor, accessory component, but the stand alone gold ores in subduction-related ultramafic intrusions are quite rare. We present in this paper new results of detailed electron microscope investigation of Au-bearing alloys in ultramafic rocks from the Ildeus intrusion in the Stanovoy Suture Zone of Far East Russia. Our previous study of native metals and intermetallic compounds in the Ildeus rocks [36] suggests that gold is principally present as Cu-Ag-Au alloys, which differs substantially from gold mineral species observed in the porphyry copper [22,37–39] and epithermal gold-silver [6,23,26,40–42] and references therein) environments. The main goals of this paper are to (1) report new type of gold-rich mineralization associated with arc-related ultramafic-mafic intrusive complexes; (2) document textural types and compositional variations in Cu-Ag-Au alloys and associated mineral inclusions in rock-forming silicate minerals, (3) evaluate the possible mobility of various components of the natural Cu-Ag-Au alloys using heating experiments in air and (4) evaluate the compositional evolution of gold-bearing assemblages during the crustal differentiation of primary mafic melts in arc-related magmatic conduits.

2. Geologic Background and Samples

The Stanovoy Suture Zone (SSZ) is located (Figure 1a) between the southern edge of the Aldan Shield (crystalline core of the Siberian craton) and accreted terranes of the Central Asian Orogenic Belt (CAOB). The CAOB separates the East European craton to the west, Siberian Craton to the north and Tarim and North China cratons to the south (Figure 1a). The CAOB is composed of Precambrian to Mesozoic oceanic, supra-subduction and back-arc ophiolites, fragments of accretionary prisms and oceanic plateaus as well as slivers of the ancient (pre-Phanerozoic) metamorphic crystalline basement intruded by Paleozoic to Mesozoic granitoids [43–46]. The Stanovoy Suture Zone (SSZ) straddles the northeastern boundary between the CAOB and the Archean crystalline Aldan Shield of the Siberian craton (Figure 1a). The SSZ records a protracted history of Paleozoic to Early Mesozoic subduction and Late Jurassic-Early Cretaceous collision between Siberian and North Amur cratons [36]. The closure of the Mongol-Okhotsk ocean and formation of the SSZ was followed by Early Cretaceous postcollisional extension and adakitic/lamprophyric magmatism [36]. The central portion of the SSZ (the so-called Bryanta Block) is composed of Late Archean (2.86–2.75 Ga; [47]) gneisses, mafic schists and amphibolites, along with Late Proterozoic, Paleozoic and Mesozoic granitoid complexes (Figure 1b). Some mafic schists are characterized by igneous protoliths, crystallization ages of 1.93 Ga and the earliest metamorphic ages of 1.89 to 1.91 Ga [48]. Trace element geochemistry of these metabasalts suggests their derivation from subduction-type mantle sources in a Paleoproterozoic arc-continent collision zone along the southern edge of the Archean Aldan shield [47,48]. The Early Cretaceous (115–117 Ma) volcanics and coeval granitoids (Figure 1b) with adakitic affinity represent late collisional and post-collisional magmatic pulses in the SSZ developed within the post-collisional extensional or transform-type continental margin environment [36]. The entire Precambrian to Mesozoic collision-related package in the central SSZ is intruded by Mesozoic ultramafic-mafic complexes associated with magmatic Au-PGE and base metal sulfide mineralization [36]. Late Triassic (232–233 Ma) Ildeus ultramafic–mafic intrusion was emplaced into the Precambrian amphibolite-gneiss-schist terrane (Figure 1b) and is characterized by a tectonically distorted, concentrically zoned structure (Figure 1c). The inner core zones include plagioclase-bearing dunites, websterites and wehrlites, while the

outer zones are predominantly composed of various pyroxenites and minor gabbros [36]. Both plutonic cores and outer zones are intruded by pyroxenitic dikes, as well as numerous veinlets, veins and dikes of adakitic and lamprophyric composition [36]. Most rocks from the Ildeus ultramafic core are characterized by cumulate textures (locally nearly completely overprinted with low-temperature greenschist facies metamorphism) formed by variable proportions of olivine, clinopyroxene, orthopyroxene, Al-rich spinel and magnetite. Pyroxenites from the intrusion's margins are fine-grained and typically display allotriomorphic textures [36]. Intercumulus phases include amphibole and plagioclase with accessory apatite, zircon, ilmenite, magnetite and sulfide. Olivines in Ildeus ultramafic rocks exhibit some variations with respect to MgO, FeO, MnO and NiO. Olivines in dunites and plagioclase-bearing dunites exhibit very low levels of CaO, Al_2O_3, TiO_2 and Cr_2O_3, while FeO, MnO and TiO_2 are higher in websterites, wehrlites and pyroxenites [36].

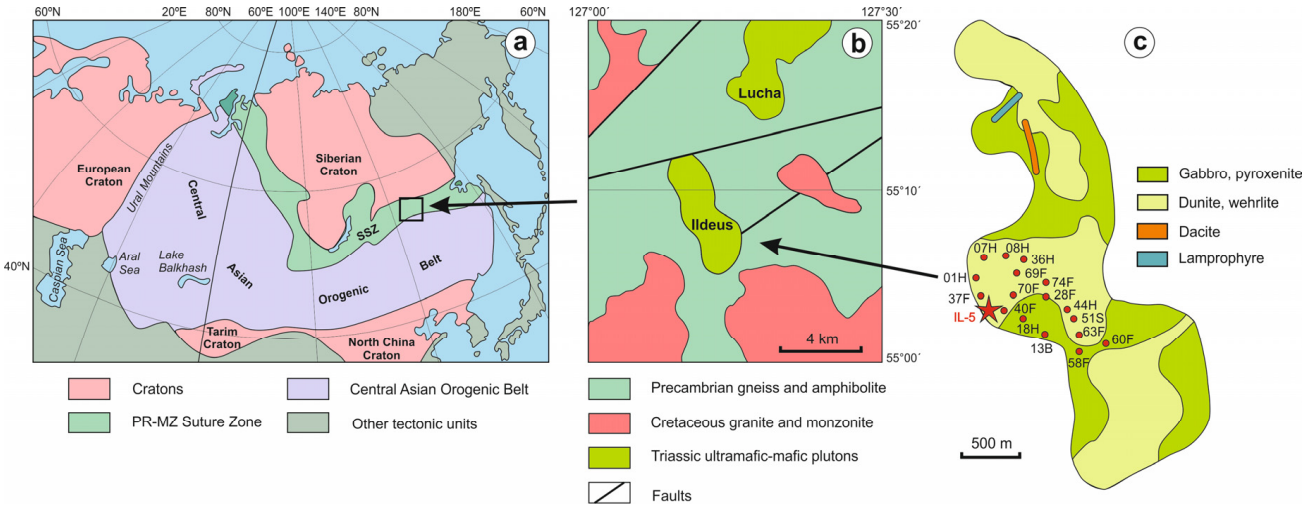

Figure 1. General tectonic setting (**a**), regional geology (**b**) and simplified geologic map (**c**) of the Ildeus intrusion, Stanovoy Suture Zone, modified after [36].

3. Methods

This study is based on ultramafic to mafic samples (n = 260) collected by the geological team of Khingan Minerals AS (Oslo, Norway) in 2018–2021, but is focused on a single websterite sample, IL-5, which exhibits the highest contents of noble metals, especially gold, within the entire collection. The collected samples provide representative coverage of principal ultramafic plutonic lithologies exposed within the central portion of the Ildeus intrusion (Figure 1c).

Thin-section studies of the ultramafic rocks from the Ildeus intrusion were carried out using an Imager A2m petrographic microscope (Carl Zeiss, Jena, Germany) at the Khabarovsk Innovative-Analytical Center (KhIAC) of Institute of Tectonics and Geophysics FEB RAS, Khabarovsk, Russian Federation. Major element compositions of selected ultramafic rocks were determined on pressed pellets using a S4 Pioneer XRF spectrometer (Bruker, Leipzig, Germany) at the KhIAC. International—LDI-3 (gabbro) and WMG-1a (mineralized gabbro)—as well as Russian DVB (basaltic andesite), DVA (andesite) and DVD (dacite), reference standards were used for calibration. The analytical uncertainty for major elements is +/−10%. Trace element abundances were measured at the KhIAC using an ELAN 9000 ICP-MS (Perkin Elmer, Woodbridge, ON, Canada), after the acid digestion of sample powder. The same set of rock reference standards (along with Perkin Elmer standard solutions PE# N9300231–9300234 for calibration) were used to monitor the analytical accuracy and precision. The accuracy was +/−5% for the trace elements with abundances of >20 ppm and +/−10% for elements with abundances of <20 ppm. The same mass-spectrometer was used to determine gold and PGE concentrations in representative ultramafic rocks from the Ildeus intrusion following the method of pre-concentration and

the separation of noble metals by Te co-precipitation as described in [49]. A systematic study of metals, intermetallic compounds and associated minerals was performed at the KhIAC using a VEGA 3 LMH TESCAN (Czech Republic) scanning electron microscope (SEM) with the Oxford X-Max 80 (GB) energy dispersive spectrometer (EDS) with the following operating conditions: accelerating voltage—20 kV; beam current—530 pA; and beam diameter—0.2 μm. A set of reference materials, including 37 natural and synthetic oxides, minerals and metallic chemical elements (Oxford/108699 # 6067), was used as reference standards; Co-standard Oxford Instruments/143100 # 9864-15 was used for routine daily instrument calibration. The EDS compositions are considered to be precise within approximately +/−0.1 mas.%. Special protocols were employed during the preparation of Ildeus ultramafic samples, which were designed to completely eliminate any possibility of the contamination of natural samples by technogenic particles, such as the handling of samples in a clean room, control over and careful assessment of composition of all materials used in sample preparation procedures (e.g., composition of diamond saw discs, grinding and polishing materials, etc.) and utilization of the "fresh fracturing" sample preparation method immediately prior to loading of the freshly broken sample surface into the sample chamber of the SEM instrument. We previously described these sample preparation methods in much detail [50]. The data set used to in this paper is based on the samples collected by the Khingan Minerals AS (Oslo, Norway; personal communication, 2021) over the entire area of the relatively well-exposed central part of the Ildeus intrusion (Figure 1c).

4. Results

4.1. Petrography of the Ildeus Intrusion

Principal petrographic features of the Ildeus intrusion are exemplified by the sample IL-5 (olivine websterite), which, on one hand, represents a typical ultramafic rock (Figure 2) within the Ildeus sequence and, on the other hand, is characterized by the highest gold and platinum-group element (PGE) contents (Au = 596.18 ppm, Pt = 0.06 ppm, Ir = 0.03 ppm, Pd = 1.44 ppm, Rh = 0.01 ppm, Ru = 0.004 ppm) among all Ildeus samples [36]. This sample was collected from the outside part of the central core at the Ildeus (Figure 1c) and can be classified as olivine websterite with a generally cumulate texture ranging from typical mesocumulate (Figure 2a,b,d,e) and orthocumulate (Figure 2f–i) to subordinate adcumulate parts (Figure 2c). Cumulate phases include olivine, orthopyroxene, clinopyroxene, aluminous spinel and magnetite (Figure 2a–i), while intercumulus is composed of amphibole (Figure 2a–e) and calcic plagioclase (Figure 2f–i).

4.2. Geochemistry of the Ildeus Intrusion

The major and trace geochemical characteristics of ultramafic rocks (dunites, plagioclase-bearing dunites, wehrlites, websterites and pyroxenites) from the Ildeus intrusion are summarized in Table 1. Intrusive rocks display significant variations in silica contents accompanied by a decrease in MgO, Cr, Ni and Co contents from dunites and wehrlites to websterites and pyroxenites (Table 1). Ildeus ultramafic rocks are characterized by a wide range of Na_2O contents (0.06–2.62 wt.%; Table 1) coupled with relatively low K_2O concentrations of 0.02–0.15 wt.% (with the exception of a single pyroxenite sample with 2.51 wt.% K_2O; Table 1). The TiO_2 contents are variable, but are generally low to moderate (0.11–1.07 wt.%), which is consistent with the overall low contents of high-field strength elements (HFSE) and variable concentrations of light rare earth (LREE) and large-ion lithophile (LILE) incompatible elements in the Ildeus intrusion (Table 1). Major element variations suggest that Ildeus rocks represent igneous cumulates formed via fractional crystallization of primitive, island arc-type magma (Figure 3a). All ultramafic plutonic rocks from the Ildeus intrusion exhibit clear HFSE depletions (Figure 3b) coupled with high LILE/LREE, LILE/HFSE ratios typical of convergent zone magmas [51,52], suggestive of their derivation from subduction-modified mantle sources [36]. Hornblende-biotite dacite

and HFSE-rich lamprophyre dikes within the Ildeus intrusion compositionally resemble typical adakites [52–54] and high-Nb basalts [52,54–56].

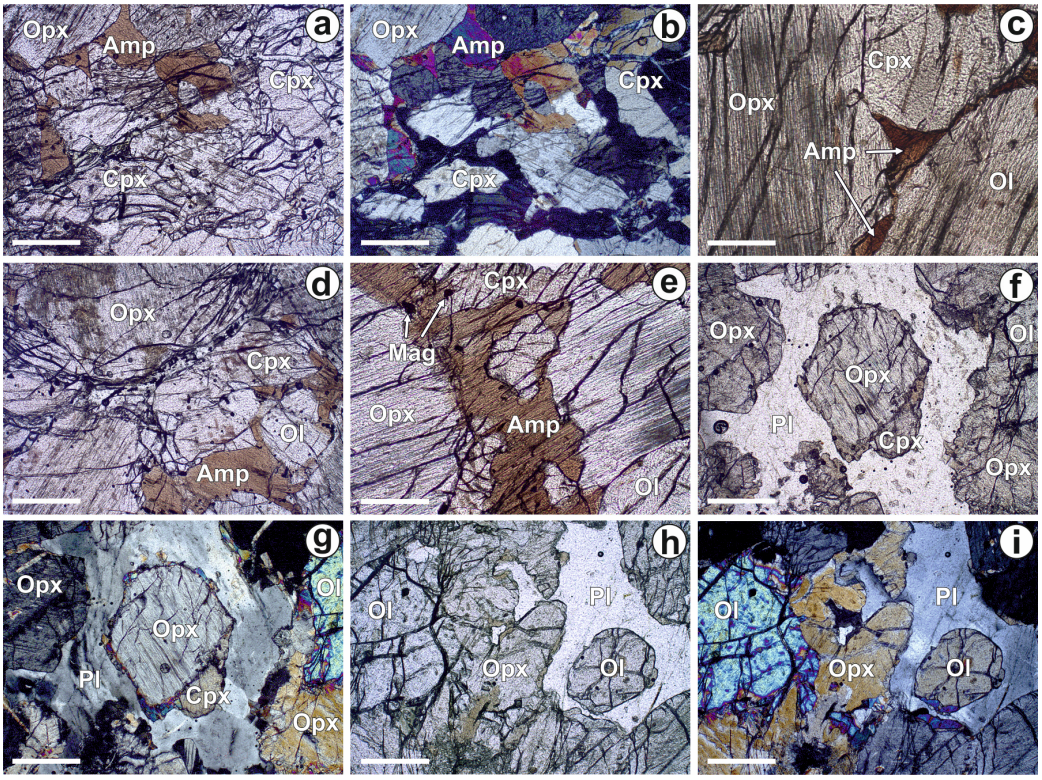

Figure 2. Petrographic features of olivine websterite IL-5. (**a**,**b**) clinopyroxene-dominated mesocumulate with amphibole as the main intercumulus phase: (**a**)—parallel nicols, (**b**)—crossed nicols. (**c**) olivine-orthopyroxene-clinopyroxene adcumulate "cemented" by amphibole intercumulus (paralel nicols). (**d**) olivine-clinopyroxene-orthopyroxene mesocumulate texture with amphibole intercumulus (parallel nicols). (**e**) detail of orthopyroxene-dominated mesocumulate texture with abundant intercumulate amphibole (parallel nicols). (**f**,**g**) orthopyroxene-dominated orthocumulate texture with plagioclase intercumulus: g—parallel nicols, (**b**)—crossed nicols. (**h**,**i**) olivine-orthopyroxene-dominated ("harzburgitic") orthocumulate texture with plagioclase intercumulus: (**h**)—parallel nicols, (**i**)—crossed nicols. Scale in all microphotographs is 20 μm.

Table 1. Major (wt.%) and trace (ppm) element geochemistry of ultramafic rocks from the Ildeus intrusion (Stanovoy suture zone, Far East Russia).

Sample	001H	007H	008H	036H	069F	070F	074F	037F	040F
Rock Type	**Pl-D**	**Pl-D**	**D**	**D**	**Pl-D**	**Pl-D**	**Pl-D**	**Whr**	**Whr**
SiO_2 (wt.%)	40.15	39.36	38.49	48.55	41.39	42.18	44.70	45.47	45.82
TiO_2	0.11	0.15	0.16	0.23	0.16	0.20	0.27	0.59	0.57
Al_2O_3	5.07	4.75	1.32	2.83	4.74	4.50	5.08	5.52	6.17
Fe_2O_3	12.12	11.38	12.40	12.84	12.55	12.93	11.80	10.59	11.83
MnO	0.16	0.17	0.18	0.18	0.18	0.23	0.23	0.18	0.19
MgO	32.29	34.38	35.17	32.84	31.72	31.16	31.52	24.25	23.61
CaO	2.85	3.19	0.52	1.94	3.54	3.14	2.34	11.20	8.91
Na_2O	0.40	1.00	0.06	0.25	0.60	0.42	0.25	0.89	0.66
K_2O	0.05	0.05	0.02	0.02	0.05	0.04	0.03	0.06	0.05
P_2O_5	0.03	0.03	0.03	0.02	0.03	0.03	0.02	0.00	0.00
LOI	6.76	5.54	11.70	0.24	5.02	5.14	3.78	1.24	2.18
Total	99.99	99.99	100.05	100.00	99.98	99.99	100.00	100.00	100.00

Table 1. *Cont.*

Sample	**001H**	**007H**	**008H**	**036H**	**069F**	**070F**	**074F**	**037F**	**040F**
Rock Type	**Pl-D**	**Pl-D**	**D**	**D**	**Pl-D**	**Pl-D**	**Pl-D**	**Whr**	**Whr**
Li (ppm)	2.09	2.09	1.13	1.80	1.72	1.17	1.13	1.18	2.40
Sc	9.21	8.74	9.91	17.96	11.18	14.14	21.41	44.36	42.12
V	48.88	37.00	42.69	67.99	44.36	64.86	83.16	135.07	159.27
Cr	2406	672.4	980.9	511.6	854.5	2496	2358	2675	1950
Co	107.18	93.4	134.2	81.45	83.03	89.56	72.73	44.66	42.00
Ni	1489	1393	1899	1291	850.98	898.4	731.12	393.1	386.0
Cu	80.01	21.16	50.58	42.42	49.67	39.74	14.07	11.10	99.47
Zn	76.57	13.13	36.78	75.31	19.29	49.83	53.95	49.10	52.62
Cs	0.08	0.01	0.03	0.08	0.11	0.10	0.21	0.07	0.05
Rb	0.65	0.29	0.46	1.22	1.11	1.25	1.25	0.65	0.69
Ba	47.16	73.30	198.1	26.03	84.31	87.85	57.65	37.60	16.63
Sr	85.36	397.8	32.15	10.95	237.5	103.75	26.20	70.48	25.53
Zr	3.04	5.15	6.38	4.27	3.27	3.10	2.61	11.16	3.77
Y	3.60	3.02	4.36	2.34	1.86	2.67	2.90	10.32	9.12
Nb	1.22	0.41	0.19	0.06	0.028	0.037	<0.001	0.28	0.24
Ta	1.47	0.54	0.14	0.075	0.093	0.065	0.023	0.42	0.32
Hf	0.12	0.16	0.20	0.15	0.12	0.13	0.13	0.61	0.31
Th	0.32	0.12	0.26	0.15	0.036	0.092	0.05	0.10	0.19
U	0.068	0.085	0.22	<0.001	0.013	0.043	0.01	<0.001	<0.001
La	3.36	2.46	4.15	0.68	0.68	0.84	0.38	1.41	0.50
Ce	7.97	5.61	10.37	1.57	1.54	1.78	1.04	5.29	2.11
Pr	0.60	0.39	0.76	0.19	0.19	0.26	0.20	1.05	0.49
Nd	3.44	2.69	3.91	0.85	0.96	1.21	0.83	5.96	3.02
Sm	0.71	0.59	0.85	0.24	0.27	0.34	0.27	1.90	1.15
Eu	0.24	0.27	0.22	0.08	0.16	0.14	0.10	0.57	0.40
Gd	0.85	0.73	1.08	0.33	0.36	0.46	0.41	2.35	1.63
Tb	0.13	0.11	0.16	0.06	0.061	0.082	0.078	0.38	0.29
Dy	0.69	0.57	0.85	0.40	0.37	0.50	0.52	2.18	1.80
Ho	0.15	0.12	0.18	0.10	0.081	0.12	0.13	0.45	0.40
Er	0.40	0.33	0.49	0.30	0.23	0.34	0.38	1.19	1.11
Tm	0.059	0.048	0.071	0.05	0.038	0.053	0.063	0.17	0.17
Yb	0.36	0.30	0.44	0.35	0.12	0.13	0.13	1.00	1.06
Lu	0.060	0.048	0.072	0.06	0.093	0.065	0.023	0.15	0.17
Sample	**IL-5**	**018H**	**028F**	**044H**	**051S**	**063F**	**013B**	**058F**	**060F**
Rock Type	**Web**	**Web**	**Web**	**Web**	**Web**	**Web**	**Pyr**	**Pyr**	**Pyr**
SiO_2 (wt.%)	48.07	50.15	51.00	46.65	47.01	48.42	46.54	47.05	46.55
TiO_2	0.49	0.49	0.58	0.31	0.31	0.65	1.07	0.46	0.30
Al_2O_3	5.50	6.45	6.61	5.45	7.04	4.22	7.23	12.21	14.48
Fe_2O_3	12.59	12.91	13.73	12.96	11.98	1.66	14.85	10.73	7.87
MnO	0.21	0.22	0.23	0.22	0.21	0.27	0.21	0.19	0.13
MgO	27.72	22.03	21.39	28.27	25.90	24.58	19.29	14.07	16.68
CaO	2.72	5.87	4.12	3.90	5.07	7.41	4.21	10.52	9.30
Na_2O	1.17	1.16	1.59	0.88	1.33	0.56	1.51	2.60	2.62
K_2O	0.09	0.07	0.16	0.10	0.09	0.06	2.51	0.15	0.15
P_2O_5	0.04	0.02	0.05	0.02	0.04	0.01	0.72	0.01	0.01
LOI	0.76	0.64	0.54	1.24	1.02	2.16	1.86	2.00	1.92
Total	99.36	100.00	100.00	100.00	100.00	100.00	100.00	100.00	100.00
Li (ppm)	1.41	3.35	3.56	1.79	1.82	2.09	9.62	5.53	3.56
Sc	24.52	39.08	22.00	22.32	20.49	49.55	13.38	29.59	18.13
V	103.39	138.77	100.84	81.18	74.51	180.71	106.00	114.48	76.34
Cr	1741	1673	1429	1782	1630	1732	483.33	910.28	709.90
Co	74.25	60.35	51.49	70.93	58.09	53.20	78.44	43.31	35.28
Ni	733.76	330.91	392.00	596.99	565.32	325.22	329.14	290.91	292.39
Cu	104.33	77.74	9.06	75.13	66.82	37.83	11.38	28.69	16.79
Zn	48.74	47.06	69.19	36.63	33.82	59.15	155.15	39.51	36
Cs	0.08	0.09	0.25	0.06	0.15	0.07	0.61	0.09	0.11

Table 1. *Cont.*

Sample	IL-5	018H	028F	044H	051S	063F	013B	058F	060F
Rock Type	**Web**	**Web**	**Web**	**Web**	**Web**	**Web**	**Pyr**	**Pyr**	**Pyr**
Rb	0.88	0.69	2.41	0.93	1.67	1.54	31.47	1.11	1.17
Ba	66.81	83.42	116.62	79.23	59.40	18.89	1521.9	74.22	93.46
Sr	150.26	135.89	189.67	99.79	174.49	27.49	311.42	520.51	625.65
Zr	14.39	9.41	5.85	6.60	7.40	6.87	13.88	3.55	3.65
Y	5.77	6.14	4.35	3.60	3.36	10.65	16.73	6.98	3.38
Nb	0.47	0.22	0.33	0.13	0.58	0.093	1.91	0.36	0.37
Ta	0.09	0.73	0.21	0.097	0.40	0.11	0.57	0.48	0.41
Hf	0.41	0.34	0.25	0.24	0.25	0.41	0.73	0.27	0.21
Th	0.25	0.085	0.24	0.059	0.22	0.13	3.37	0.19	0.11
U	1.82	0.006	<0.001	<0.001	0.01	0.041	0.71	0.047	0.064
La	1.77	1.12	1.64	0.73	1.14	1.21	36.09	1.45	1.28
Ce	4.39	2.91	3.69	1.92	2.57	4.18	75.60	3.88	2.97
Pr	0.59	0.13	0.50	0.26	0.34	0.73	8.94	0.51	0.38
Nd	2.76	2.10	2.20	1.32	1.53	4.13	33.07	2.77	1.87
Sm	0.75	0.68	0.57	0.39	0.41	1.41	5.53	0.92	0.49
Eu	0.28	0.30	0.27	0.18	0.19	0.49	1.80	0.49	0.38
Gd	1.01	0.98	0.75	0.57	0.57	2.00	6.02	1.32	0.67
Tb	0.16	0.17	0.13	0.11	0.10	0.35	0.72	0.23	0.11
Dy	1.02	1.07	0.78	0.66	0.62	2.10	3.34	1.40	0.67
Ho	0.22	0.24	0.18	0.15	0.14	0.46	0.64	0.31	0.15
Er	0.67	0.68	0.53	0.45	0.42	1.24	1.74	0.84	0.41
Tm	0.10	0.11	0.09	0.072	0.068	0.18	0.23	0.13	0.062
Yb	0.67	0.69	0.56	0.45	0.44	1.13	1.40	0.76	0.39
Lu	0.11	0.11	0.092	0.12	0.08	0.17	0.21	0.12	0.063

Rock types: D—dunite, Pl-D—plagioclase-bearing dunite, Web—websterite, Whr—wehrlite, Pyr—pyroxenite. Analysis IL-5 is from [36]. Sample location is shown in Figure 1c.

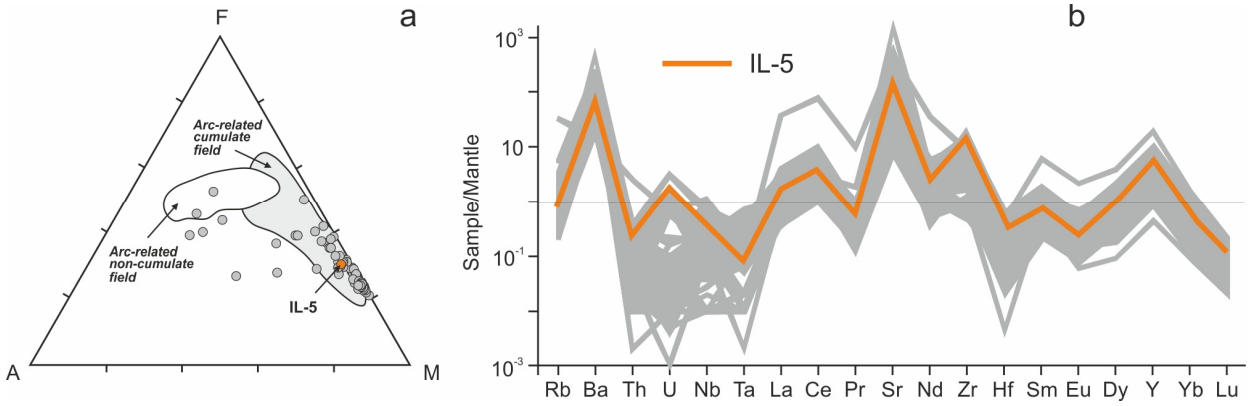

Figure 3. Geochemistry of ultramafic cumulate rocks from the Ildeus intrusion reflecting their suduction-related tectonic setting. (**a**) A (Na_2O+K_2O)—F (total FeO)—M (MgO) diagram for Ildeus intrusion. Fields of arc-related cumulate and arc-related non-cumulate plutonic rocks are from [57] with modifications from [36]. (**b**) Primitive mantle-normalized trace-element patterns for plutonic rocks from the Ildeus intrusion (54 samples). Primitive mantle normalizing values are from [58]. Please note that olivine websterite IL-5 is characterized by arc-related ultramafic cumulate chemistry, including well-defined HFSE (Nb, Ta and Hf) depletions in (**b**), typical of primitive convergent zone magmas [51,52].

Most plutonic rocks within Ildeus intrusion, including sample IL-5, carry disseminated sulfide mineralization composed of primary pentlandite, Co-pentlandite, chalcopyrite, Ni-chalcopyrite and bornite along with secondary/metasomatic assemblages including digenite, heazlewoodite, pyrite, Ni-pyrite, sphalerite, Ni-sphalerite, millerite and Cu- Pb sulfide [36]. Other notable mineral phases in the Ildeus intrusion include halides (NaCl),

sulfosalts (gersdorffite, gratonite, arsenopyrite), sulfates (barite), native metals (W, Pt, Zn, Bi, Au and Ag) and various Ni-Cu-Zn-Ag-Au, Cu-Zn-Sn, Pb-Sb, Fe-Pt, Ni-Rh- Pt and Pd-Pt alloys [36].

4.3. Gold Alloys in the Ildeus Intrusion

Figure 4 presents the statistical distribution of gold in the rocks of Ildeus intrusion based on the samples collected by the Khingan Minerals AS (personal communication, 2021) over the entire area of its relatively well-exposed central part (location of some samples listed in Table 1 is shown in Figure 1c). The general character of the distribution of gold contents in the ultramafic rocks of the Ildeus intrusion (Figure 4) suggests that at least a third of all of the samples is characterized by gold from grades in the range of 10 to 100 ppb, while approximately 10% of samples display gold grades in excess of 100 ppb, which is significantly higher than the gold clark values in ultramafic rocks (6–7 ppb) [59,60] and average gold content of the Earth's crust (around 5 ppb) [61–63]. This significant enrichment of ultramafic rocks from the Ildeus intrusion in Au (Figure 4) suggests that gold in these cumulate ultramafic rocks may form its own mineral phases.

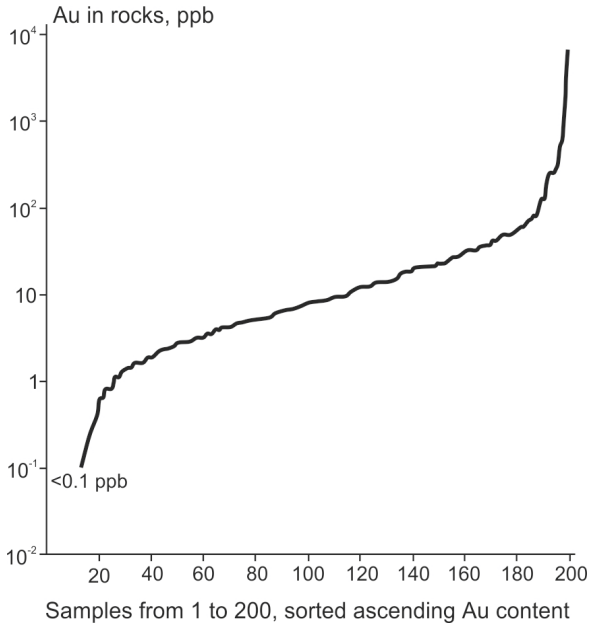

Figure 4. Statistical distribution of gold in the Ildeus intrusion.

Detailed SEM-EDA studies of Au-rich ultramafic samples from the Ildeus intrusion have established the ubiquitous presence of small (1–15 μm) micro-inclusions of gold-, silver- and copper-bearing alloys in rock-forming minerals from these rocks (Figure 5). These microinclusions display predominant Cu-Ag-Au compositions in association with olivine, orthopyroxene and amphibole (Figure 5a,b). Some gold-bearing particles in orthopyroxene are mostly composed of Au with Ag (up to 7 wt.%), Ni (up to 8.2 wt.%), Cu (up to 37 wt.%), and Zn (up to 8.8 wt.%) (Figure 5c,d). Silver grains with variable copper admixture (Figure 5e; Cu up to 7.7 wt.%) were observed in olivine as well as in the larger orthopyroxene grain intersected by very thin (1–3 μm) chalcopyrite veinlets (Figure 5f).

Numerous relatively large (50–200 μm) particles of Au-bearing intermetallic compounds were recovered from olivine websterite sample IL-5 (most enriched in Au = 596.18 ppm) by rough crushing and gravitational separation, following the general methods described in [50]. These are irregularly shaped, partially facetted Cu-Ag-Au grains with multiple crystalline inclusions and specific inner structure (Figure 6).

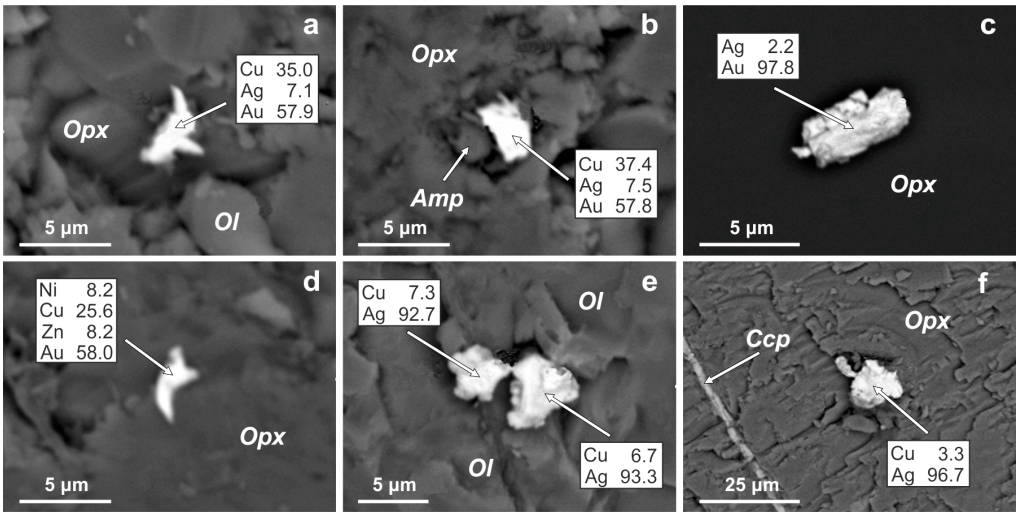

Figure 5. Small inclusions of copper-, silver- and gold-bearing alloys in rock-forming minerals from the ultramafic rocks of the Ildeus intrusion. (**a**,**b**) Cu-Ag-Au alloys associated with olivine and orthopyroxene (**a**) and orthopyroxene and amphibole (**b**). (**c**) Ag-Au alloy included in orthopyroxene. (**d**) Ni-Zn-Cu-Au alloy included in orthopyroxene. (**e**) Cu-Ag alloy included in olivine. (**f**) Cu-Ag alloy included in orthopyroxene along with veinlet composed of chalcopyrite. Mineral abbreviations: Ol—olivine, Opx—orthopyroxene, Amp—amphibole, Ccp—chalcopyrite.

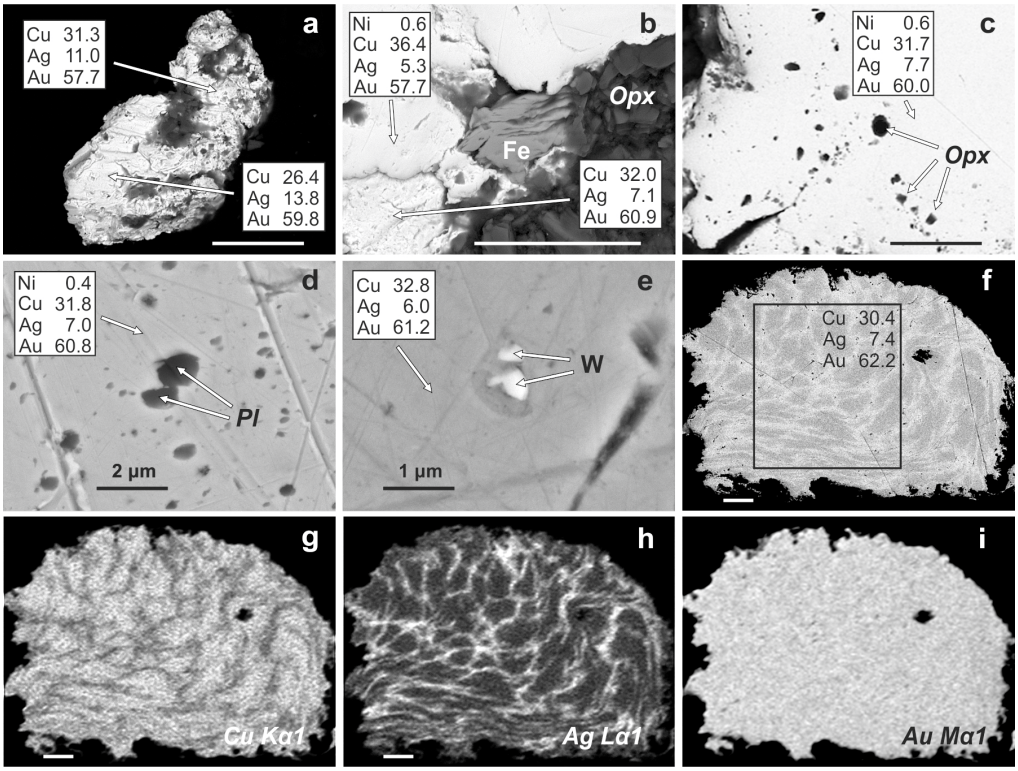

Figure 6. General view (**a**) and polished cross-sections (**b**–**i**) of gold-bearing particles from the olivine websterite IL-5. (**b**) Cu-Ag-Au(±Ni) alloys co-existing with native iron and orthopyroxene. (**c**–**e**) inclusions of orthopyroxene (**c**), plagioclase (**d**) and native tungsten (**e**) in Cu-Ag-Au(±Ni) alloys. (**f**–**i**) cross-section through a 180 μm grain of Cu-Ag-Au alloy with distinct cellular ("honeycomb") exsolution structure: (**f**)—high-contrast BSE image. Rectangle shows area scanned for the estimation of integrated bulk chemical composition. (**g**–**i**) individual distribution maps for copper (**g**), silver (**h**) and gold (**i**) based on their characteristic radiation. Scale in all microphotographs, where it is not specifically stated, is 20 μm.

Some Au-bearing particles are intergrown with native iron and orthopyroxene (Figure 6b) and occasionally contain micro-inclusions of orthopyroxene (~1–3 µm; Figure 6c), Ca-Na plagioclase (0.5–2 µm; Figure 6d) and native tungsten (less than 1 µm; Figure 6e). SEM-EDS analyses of the surface of large Cu-Ag-Au grains display the following compositional variations: Cu from 26.4 to 45.0 wt.%, Ag from 4.0 to 13.8 wt.% and Au from 51.1 to 62.5 wt.% averaging Cu = 32.9 wt.%, Ag = 7.9 wt.% and Au = 59.0 wt.%. Nine analyses include 0.3–0.8 wt.% Ni. The SEM-EDS analyses of polished cross-sections through large Cu-Ag-Au particles exhibit roughly the same results, as follows: Cu from 27.3 to 36.6 wt.%, Ag from 3.7 to 13.0 wt.% and Au from 58.0 to 63.2 wt.% averaging Cu = 32.4 wt.%, Ag = 6.9 wt.% and Au = 60.8 wt.%. All analyzed compositions of Cu-Ag-Au grains are plotted in the ternary Cu-Ag-Au diagram in Figure 7.

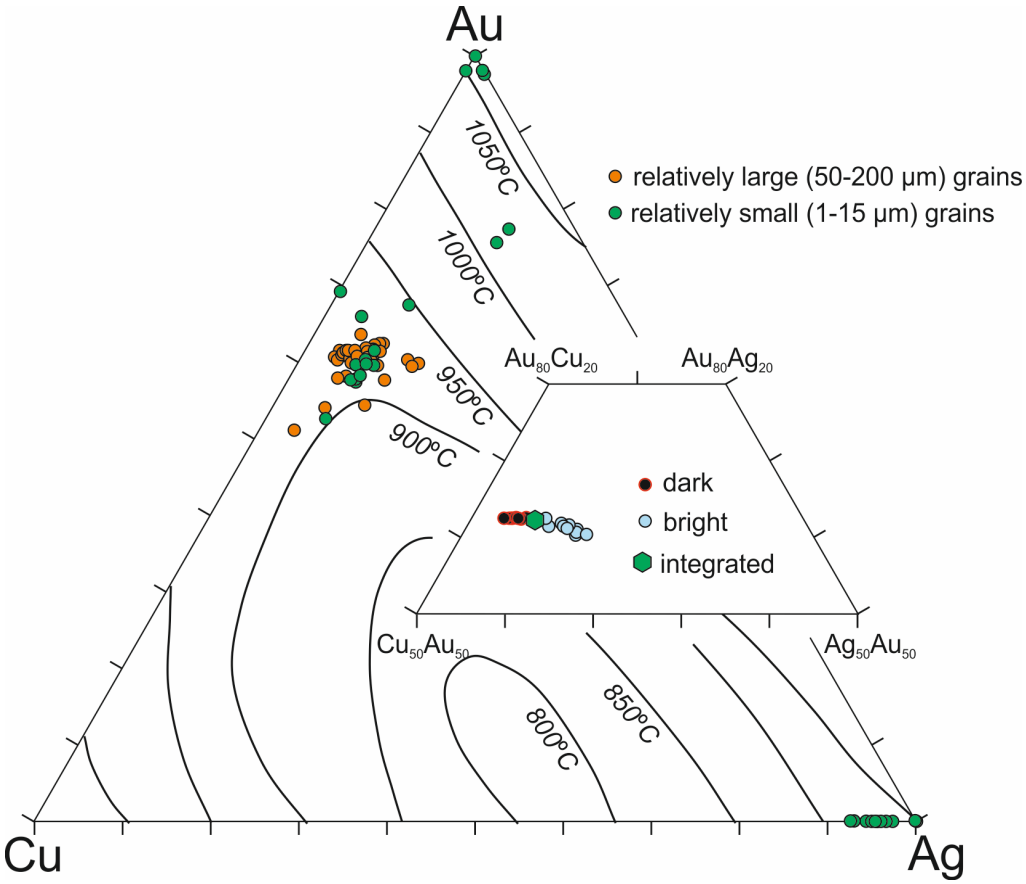

Figure 7. Composition of Cu-Ag-Au compounds recovered from olivine websterite IL-5 plotted on ternary phase diagram modified after [64] with additions from [65]. Solid lines depict liquidus temperatures at different end-member compositions. Please see text for additional explanation.

Although cross-sections (cuts) through individual Cu-Ag-Au grains appear to be texturally homogeneous in reflected light and during standard SEM studies, EDS analyses of different points on polished surfaces reveal distinct compositional variations. In order to resolve these compositional heterogeneities, we carried out detailed high-resolution SEM-EDS studies of this area. First of all, we strived to obtain the highest contrast image, which clearly revealed the co-existence of dark and bright zones in these grains (Figure 6f). The difference in BSE colors typically indicate a difference in chemical composition, which was confirmed by the construction of individual elemental maps, which are presented in Figure 6g (copper), Figure 6h (silver) and Figure 6i (gold). These BSE elemental maps emphasized presence of dark and bright areas with difference in color representing fine-scale compositional variations in individual metal concentrations and different compositional zones (different colors in BSE images in Figure 6f–i) displaying some typical plastic defor-

mation features. The composition of individual zones with different (dark versus bright) colors is estimated using both an EDS analysis of the selected surface points and elemental maps obtained through surface areal scanning. The results are summarized in the inset in Figure 7, where «dark» data points correspond to measurements within dark zones and «bright» data points reflect results from ribbon-like areas between the dark-colored zones in BSE images in Figure 6f,h,i. Copper concentrations within the dark areas vary from 30.4 to 33.9 wt.%, silver—from 3.8 to 7.2 wt.% and gold—from 62.3 to 62.7 wt.% averaging Cu = 32.4 wt.%, Ag = 5.1 wt.% and Au = 62.5 wt.% (total of 10 SEM-EDS analyses). Copper content in bright areas ranges from 25.8 to 29.4 wt.%, silver—from 8.6 to 14.0 wt.% and gold—from 60.2 to 62.3 wt.% averaging 27.5 wt.% Cu, 11.4 wt.% Ag and 61.1 wt.% Au (total of 9 SEM-EDS analyses). Based on these results, dark areas are enriched in copper (+4.9 wt.% Cu on average) and depleted in silver (−6.3 wt.% Ag on average) at a nearly constant Au content in reference to the bright-colored zones. The integrated bulk chemical composition of this grain is estimated by spectral scanning of a 150 μm by 150 μm area (rectangle on Figure 6f): Cu = 30.4 wt.%, Ag = 7.4 wt.% and Au = 62.2 wt.%, green polygon symbol in the inset in Figure 7.

4.4. Heating Experiments on Cu-Ag-Au Alloys

In order to evaluate the potential mobility of various components (specifically copper) of Cu-Ag-Au alloys under low-temperature hydrothermal conditions, we conducted heating experiments with large Cu-Ag-Au grains from sample IL-5 in the presence of atmospheric oxygen. A 24 h exposure at 300 °C resulted in the formation of the 5–8 μm cuprite crust on the Cu-Ag-Au grain, while its peripheral parts became depleted in copper and enriched in silver and gold (Figure 8). The removal of copper from these structural pores is visible in Figure 8.

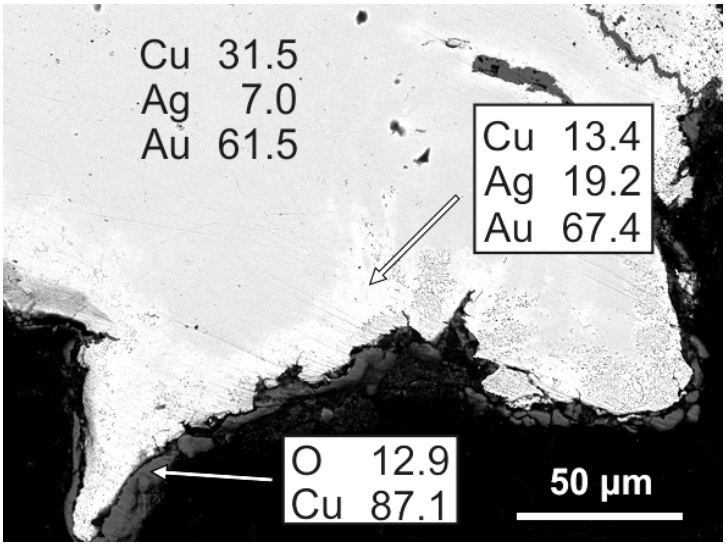

Figure 8. Oxidation of peripheral zones of natural Cu-Ag-Au grain from sample IL-5 exposed to the 300 °C temperature for 24 h in presence of the atmospheric oxygen (open air experiment).

5. Discussion

5.1. Petrological and Geochemical Constraints on the Origin of the Ildeus Intrusion

The petrologic and geochemical evidence presented above and summarized in [36] identifies plutonic rocks from the Ildeus intrusion as ultramafic cumulates from primitive convergent zone magma (cf. Figures 2 and 3). Peridotites, webesterites, wehrlites and pyroxenites display typical mesocumulate, orthocumulate and adcumulate textures composed of olivine, orthopyroxene and clinopyroxene as major cumulus phases and amphibole, plagioclase and magnetite as principal intercumulus phases. Ildeus ultramafic rocks, for the most part, plot in the arc-related cumulate field and form a typical calc-alkaline com-

positional trend on the AFM diagram (Figure 3a). The arc-related character of the Ildeus intrusion is further accentuated by primitive mantle-normalized trace element patterns with distinct LILE (Rb, Ba) enrichements and HFSE (Nb, Ta, Hf) depletions (Figure 3b) typical of convergent zone magmas [51–53].

5.2. Physico-Chemical Conditions of Cu-Ag-Au Alloys Formation

The compositional data summarized above in Figure 7 indicate that solidification of Cu-Ag-Au alloys with compositional ranges of Cu, Ag and Au metallic components, observed in the grains that were analyzed in this study, occurs within the temperature range of 900–950 °C [64]. Textural and compositional features presented in Figures 6 and 7 suggest that nucleation and initial consolidation of these Au-bearing alloys into a separate mineral phase occurred at even higher temperatures that correspond to their liquid state during the crystallization of principal rock-forming minerals (e.g., olivine, pyroxene and plagioclase) within the Ildeus intrusion. This is consistent with the occurrence of olivine and orthopyroxene micro-inclusions in Cu-Ag-Au alloys (Figure 6c,d) and the general lamellar shape of many large Cu-Ag-Au grains, which is indicative of their solidification in the intergranular spaces between the rock-forming silicate minerals. Textural data indicate that the incorporation of microparticles of highly refractory native tungsten (Figure 6e) most probably occurred when the Cu-Ag-Au alloys were still in the liquid state. The preservation of the original crystalline shape and initial composition of native tungsten micro-inclusions (no alloying between W, Cu, Ag and Au has been observed) during transformation of Cu-Ag-Au alloys from liquid into solid state was possible due to the complete lack of physical and chemical interactions between crystalline tungsten and solid and liquid gold [66], silver [67] and copper [68]. Additionally, the observed meshy texture in some grains (Figure 6f, lower portion of the image) can be possibly explained either by shock deformation during crushing or by plastic deformations during high-temperature processes involved in the formation of these alloys.

Another controlling factor, which can greatly influence the formation of Cu-Ag-Au alloys during the crustal fractionation of convergent zone magmas, is low oxygen fugacity. Although current petrologic models suggest that most arc magmas and their ultramafic cumulates are variably oxidized in comparison to mid-ocean ridge basalts (MORB) [69,70], some recently published data indicate that modern and fossil subduction zones are characterized by substantial redox heterogeneity, with some portions of the subducted slab and mantle wedge associated with reduced conditions (negative ΔFMQ values) [36,50,71,72]. Moreover, various geochemical proxies suggest that early fractionates of convergent zone magmas (primitive arc cumulates) can be generally reduced (similar to MORB) and increase in oxygen fugacity during their further crustal magmatic differentiation [73,74]. Very low oxygen fugacity conditions during the formation of Cu-Ag-Au alloys in ultramafic samples from the Mesozoic Stanovoy subduction zone were reconstructed on the basis of the Cu-Ag-Au alloy co-existence with native iron (Figure 6b), as well as for a general consideration of the Cu-O phase diagram, which suggests that the Cu-Ag-Au alloys with chemical compositions observed in the Ildeus rocks are stable at the oxygen fugacity levels of $Log(O_2) < -4$ [65]. Previously, we found compositionally similar Cu-Ag-Au alloys in pyroclastic rocks from the Lesser Khingan iron district (Russian Far East), where they are present as micro-spherules indicating their solidification in a low density media (e.g., water or air) [65,75] as opposed to the Cu-Ag-Au alloys in the Ildeus intrusion, which crystallized together with rock-forming and accessory minerals [36]. Oxygen fugacity estimates for Cu-Ag-Au alloys from the Lesser Khingan pyroclastic rocks are in the range of −2 to −4 [65]. The oxygen fugacity increase in the Cu-Ag-Au ternary system will immediately lead to the occurrence of copper oxide (cuprite) represented by the immiscible liquid or distinctive skeletal crystals [65]. The absence of this petrologic phenomenon in the Cu-Ag-Au grains from the Ildeus intrusions indicates low fO_2 conditions during their formation and the crystallization of Ildeus parental magma. Based on the observations and experiments summarized in [65], the overprinting of primary Au-bearing intermetallic compounds with

highly oxidized (estimated ΔQFM > 1) mesothermal and epithermal hydrothermal processes should result in the pervasive oxidation of magmatic Cu-Ag-Au alloys accompanied by copper loss and enrichment in gold and silver components. Experimental heating of Cu-Ag-Au particles in air suggest that such oxidation, Au-Ag enrichment and the extraction of copper into a surficial oxide film initiates at approximately 250 °C. The final product of this advanced (hydro)thermal oxidation process in nature is represented by the Cu-poor, Au- and Ag-enriched grains in some ultramafic rocks from the Ildeus intrusion affected by later-stage hydrothermal alteration (Figures 5c–e and 7).

To further evaluate this petrologic scenario, we use our experimental results presented above in Section 4.3. To understand this decomposition phenomenon, we used schematic quasi-binary sections at constant caratage of the gold-silver-copper ternary phase diagram compiled by Rapson [76]. The gold content in the studied Cu-Ag-Au grains from the Ildeus intrusion averages around 62.2 wt.% (based on the integrated SEM-EDS scanning of a cross-section through the large Cu-Ag-Au grain (Figure 6f)), which corresponds to a 14 Carat quasibinary section presented in Figure 9. The actual position of these compositions on the 14 Carat quasi-binary section is determined by the so-called Ag′-factor, which is defined by the following equation: Ag′ = Ag (wt.%)/(Ag (wt.%) + Cu (wt.%) × 100% [76]. Ag′-factor for large Cu-Ag-Au grains in olivine websterite IL-5 equals 19.6. The cooling evolutionary path for these Cu-Ag-Au alloy compositions on the 14 Carat quasi-binary section is shown by the dashed line, which reaches the immiscibility gap area around the temperatures of 540–550 °C (Figure 9). The two separate solid phases within the immiscibility gap in Figure 9 (e.g., Ag-rich and Cu-rich) most probably form the cellular ("honeycomb") structure observed in some larger Cu-Ag-Au grains in olivine websterite from the Ildeus cumulate sequence (Figure 6f).

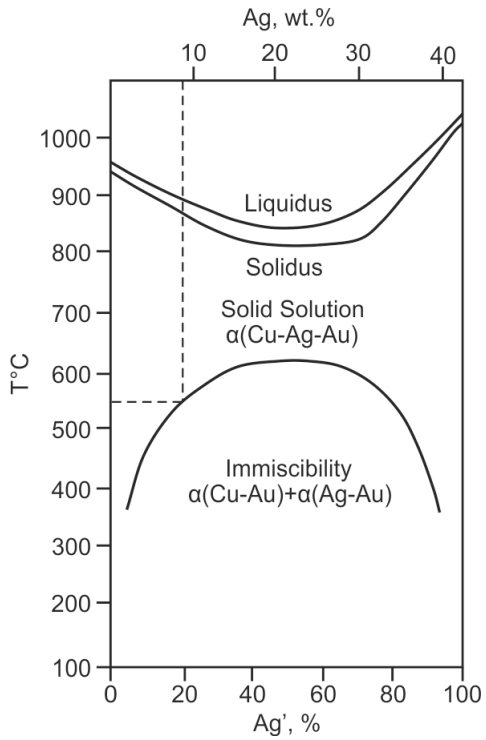

Figure 9. 14 Carat schematic quasi-binary section of the gold-silver-copper ternary phase diagram according to [76]. Ag′-factor is Ag′ = Ag/(Ag + Cu) × 100. Dashed line depicts typical cooling pattern for Cu-Ag-Au grains from the Ildeus intrusion and the corresponding temperature of the inception of exsolution of initial homogenous Cu-Ag-Au alloy into two separate phases.

5.3. Geologic Conditions of the Formation of Cu-Ag-Au Alloys in Magmatic Systems

The textural and compositional characteristics of Cu-Ag-Au alloys in ultramafic rocks of the Ildeus intrusion indicate that gold-bearing compounds in cumulate fractionates from primitive arc magmas differ in chemical composition from gold grains in typical upper-crustal epithermal and porphyry mineralized systems [22,26,27,37,38,41–44,77–79]. These textural and compositional differences, as well as the association of magmatic gold alloys with high-temperature rock-forming silicate minerals and other metallic phases (such as iron in Figure 6b and tungsten in Figure 6e), also suggest drastically different evolutionary pathways for gold formation in the upper mantle and deeper crustal settings (close to the magma source and within deep crustal magmatic conduits) in comparison with the shallow porphyry, mesothermal and epithermal environments of gold transportation and deposition.

The relatively rarity of the native gold with these specific "magmatic" compositions of $Cu_{\sim 30}Ag_{\sim 10}Au_{\sim 60}$ can be most probably explained by the instability of this Au-bearing alloy under oxidized conditions of mesothermal and epithermal hydrotherms, which typically results in the almost instantaneous removal of the copper component. Consequently, the search for "primary magmatic" gold should concentrate on mineralized systems hosted in deep-seated, relatively reduced crustal and mantle rocks, which were not previously subjected to the upper crustal oxidation. Primary magmatic gold particles (clustering around $Cu_{30}Ag_{10}Au_{60}$ compositions) were documented in pyroclastic rocks associated with iron mineralization in the Lesser Khingan Range [65], mantle wedge peridotite xenoliths from Kamchatka [50] and adakites from the Stanovoy suture zone [54]. Oen and Kieft [80] reported native gold particles with 11 wt.% copper in the hydrothermal Ni-Co arsenide ores from the chromitites in the serpentinized Beni Bousera Ultramafic Massif (Morocco).

Gold and other noble metal enrichments were previously reported for both sub-arc mantle sources [19,50,81–83] and subduction-related crustal magmatic conduits [19,36], as well as primitive basaltic and andesitic magmas in volcanic arcs [54,84,85]. The distribution of gold in differentiated arc-related plutonic and volcanic suites suggests that Au behaves as an incompatible element during the fractionation of primitive convergent zone magmas [36,54,85,86]. This results in the accumulation of precious metals, especially gold, in evolved, late-stage intermediate to felsic residual liquids and contemporaneous enrichment of residual melts in subduction zones in sulfur and magmatic sulfides [20,28,87,88]. This is consistent with the ubiquitous presence of late-stage magmatic barite in evolved pyroxenites from the Ildeus intrusion [36] as well as adakitic dikes associated with Triassic plutonic complexes in the central segment of the Stanovoy suture zone [56]. In some cases, sulfur is present in convergent zone magmas during various stages of their evolution beneath arc volcanoes [89,90], while on other occasions, sulfides are formed in differentiating arc melts through the assimilation of graphite-bearing crustal rocks and reduction in the initially oxidized arc basalt magma [87]. Under all these petrologic scenarios, gold is accumulated in differentiated arc basalts and late-stage residual magmatic liquids in subduction zone environments to the point of metal saturation during the advanced fractionation of convergent zone magmas, which may, in turn, trigger the formation of gold-rich globules and micro-nuggets [20,65,75] as well as the crystallization of gold-bearing intermetallic compounds [36,54] during late-stage magmatic differentiation processes in the upper island-arc crust. According to several experimental studies, the crystallization of noble metal compounds (assemblages) during crustal differentiation of convergent zone magmas occurs under oxidized conditions, which is inconsistent with our observations from natural systems in subduction-related environments within the Lesser Khingan and Stanovoy Ranges of the Russian Far East [19,36,65,75]. In particular, gold-bearing alloys in the Ildeus intrusion co-exist with a wide range of native metals (Pt, W, Bi, Pb, Zn, Au, Ag) and intermetallic compounds (Fe-Pt, Ni-Rh-Pt, Pd-Pt, Cu-Ag-Au, Cu-Ag, Ni-Cu-Zn-Ag-Au, Cu-Zn-Ag, Cu-Zn-Au, Cu-Sn, Cu-Zn-Sn, Pb-Sb) indicating reduced conditions during the development of crustal magmatic conduits in the Triassic Stanovoy subduction zone [36]. Our data from the Ildeus intrusion suggest that, besides the influence of pressure and

temperature, variations in the redox conditions between deep lithosphere and shallow, oxidized upper crust in subduction-related settings [36,70,71,73], where gold and other ore metals are usually deposited in the porphyry and epithermal environments [6,26,91,92] will also play an important role in the modification of Au-bearing alloys under a range of crustal conditions.

6. Conclusions

Rocks of the Triassic (232–233 Ma) Ildeus intrusion in the Stanovoy suture zone represent ultramafic cumulates from the primitive convergent zone magma. lldeus ultramafic rocks are enriched in Au and contain micro-particles of Cu-Ag-Au alloys. These alloys correspond to the $Cu_{\sim 60}Ag_{\sim 10}Au_{\sim 30}$ compositions that were previously reported from the explosive pyroclastic rocks in the Khingan iron district, mantle wedge peridotites in Kamchatka and Mesozoic adakites from the Stanovoy subduction system. The $Cu_{\sim 30}Ag_{\sim 10}Au_{\sim 30}$ compositions most probably represent primary-magmatic gold alloys formed during the crustal differentiation of a convergent zone magma. Some Au-alloys display honeycomb-like structure with alternating Cu-rich and Cu-poor zones. Heating experiments in air confirmed the loss of copper from $Cu_{\sim 30}Ag_{\sim 10}Au_{\sim 60}$ alloy at temperatures of 250–300 °C, which are typical of oxidized hydrothermal environments in the upper crust. The resultant Cu-free native gold compositions in the Ildeus intrusion are comparable to native gold mineralization in oxidized porphyry-mesothermal-epithermal settings. Subduction-related mineralized igneous systems with the primary magmatic Cu-Ag-Au alloys provide efficient means of gold transport from the deep lithospheric sources to the upper crustal environments. Consequently, the primary magmatic Cu-Ag-Au alloys can be potentially used as pathfinders for base and noble metal mineralization associated with intrusive formations at the convergent plate margins.

Author Contributions: Conceptualization, N.B. and P.K.; methodology, N.B. and N.K. (Natalia Konovalova); validation, N.B. and P.K.; formal analysis, N.B., P.K., N.K. (Natalia Konovalova) and N.K. (Nikita Kepezhinskas); investigation, N.B., P.K. and N.K. (Natalia Konovalova); resources, N.B., P.K. and N.K. (Nikita Kepezhinskas); data curation, N.B., P.K., N.K. (Natalia Konovalova) and N.K. (Nikita Kepezhinskas); writing—original draft preparation, N.B. and P.K.; writing—review and editing, N.B., P.K. and N.K. (Nikita Kepezhinskas); visualization, N.B. and P.K.; supervision, N.B. and P.K.: project administration, N.B. and P.K. All authors have read and agreed to the published version of the manuscript.

Funding: This research received no external funding.

Institutional Review Board Statement: Not applicable.

Informed Consent Statement: Not applicable.

Data Availability Statement: Not applicable.

Acknowledgments: We acknowledge continuous support from the Khingan Minerals AS (Oslo, Norway) and its Chairman of the Board, Tore Birkeland for our work in the Stanovoy suture zone.

Conflicts of Interest: The authors declare no conflict of interest.

References

1. Sawkins, F.J. *Metal Deposits in Relation to Plate Tectonics*; Springer: Berlin, Germany, 1984; 325p.
2. Sillitoe, R.H. Gold deposits in Western Pacific island arcs: The magmatic connection. In *The Geology of Gold Deposits: The Perspective in 1988*; Keays, R.R., Ramsay, W.R.H., Groves, D.I., Eds.; The Society of Economic Geology: Littleton, CO, USA, 1989; pp. 274–291.
3. Hedenquist, J.W.; Lowenstern, J.B. The role of magmas in the formation of hydrothermal ore deposits. *Nature* **1994**, *370*, 519–527. [CrossRef]
4. Mungall, J.E. Roasting the mantle: Slab melting and the genesis of major Au and Au-rich Cu deposits. *Geology* **2002**, *30*, 915–918. [CrossRef]
5. Herrington, R.; Maslennikov, V.; Zaykov, V.; Seravkin, I.; Kosarev, A.; Buschmann, B.; Orgeval, J.-J.; Holland, N.; Tesalina, S.; Nimis, P.; et al. 6: Classification of VMS deposits: Lessons from the South Uralides. *Ore Geol. Rev.* **2005**, *27*, 203–237. [CrossRef]

6. Simmons, S.F.; Brown, K.L. Gold in magmatic hydrothermal solutions and the rapid formation of a giant ore deposit. *Science* **2006**, *314*, 288–291. [CrossRef] [PubMed]
7. Sillitoe, R.H. Major gold deposits and belts of the North and South American cordillera: Distribution, tectonomagmatic settings, and metallogenic considerations. *Econ. Geol.* **2008**, *103*, 663–687. [CrossRef]
8. Mercier-Langevin, P.; Hannington, M.D.; Dube, B.; Becu, V. The gold content of volcanogenic massive sulfide deposits. *Miner. Depos.* **2010**, *46*, 509–539. [CrossRef]
9. De Ronde, C.E.J.; Massoth, G.J.; Buttterfield, D.A.; Christenson, B.W.; Ishibashi, J.; Ditchburn, R.G.; Hannington, M.D.; Brathwaite, R.L.; Lupton, J.E.; Kamenetsky, V.S.; et al. Submarine hydrothermal activity and gold-rich mineralization at Brothers Volcano, Kermadec Arc, New Zealand. *Mineral. Depos.* **2011**, *46*, 541–584. [CrossRef]
10. Muntean, J.L.; Cline, J.S.; Simon, A.C.; Longo, A.A. Magmatic-hydrothermal origin of Nevada's Carlin-type gold deposits. *Nat. Geosci.* **2011**, *4*, 122–127. [CrossRef]
11. Richards, J.P. Magmatic to hydrothermal metal fluxes in convergent and collided margins. *Ore Geol. Rev.* **2011**, *40*, 1–26. [CrossRef]
12. Groves, D.I.; Zhang, L.; Santosh, M. Subduction, mantle metasomatism, and gold: A dynamic and genetic conjunction. *Geol. Soc. Amer. Bull.* **2020**, *132*, 1419–1426. [CrossRef]
13. Sun, W.D.; Arculus, R.J.; Kamenetsky, V.S.; Binns, R.A. Release of gold-bearing fluids in convergent margin magmas prompted by magnetite crystallization. *Nature* **2004**, *431*, 975–978. [CrossRef] [PubMed]
14. Nadeau, O.; Williams-Jones, A.E.; Stix, J. Sulphide magma as a source of metals in arc-related magmatic hydrothermal ore fluids. *Nat. Geosci.* **2010**, *3*, 501–505. [CrossRef]
15. Jégo, S.; Pichavant, M. Gold solubility in arc magmas: Experimental determination of the effect of sulfur at 1000 °C and 0.4 GPa. *Geochim. Cosmochim. Acta* **2012**, *84*, 560–592. [CrossRef]
16. Zajacz, Z.; Candela, P.; Piccoli, P.M.; Walle, M.; Sanchez-Valle, C. Gold and copper in volatile saturated mafic to intermediate magmas: Solubilities, partitioning, and implications for ore deposit formation. *Geochim. Cosmochim. Acta* **2012**, *91*, 140–159. [CrossRef]
17. Li, J.-L.; Gao, J.; John, T.; Klemd, R.; Su, W. Fluid-mediated metal transport in subduction zones and its link to arc-related giantore deposits: Costraints from a sulfide-bearing HP vein in lawsonite eclogite (Tianshan, China). *Geochim. Cosmochim. Acta* **2013**, *120*, 326–362. [CrossRef]
18. Edmonds, M.; Mather, T.A.; Liu, E.J. A distinct metal fingerprint in arc volcanic emissions. *Nat. Geosci.* **2018**, *11*, 790–794. [CrossRef]
19. Kepezhinskas, P.; Kepezhinskas, N.; Berdnikov, N. Gold, platinum and palladium enrichments in arcs: Role of mantle wedge, arc crust and halogen-rich slab fluids. *E3S Web Conf.* **2019**, *98*, 08010. [CrossRef]
20. Kamenetsky, V.S.; Zelenski, M. Origin of noble-metal nuggets in sulfide-saturated arc magmas: A case study of olivine-hostedsulfide melt inclusions from the Tolbachik volcano (Kamchatka, Russia). *Geology* **2020**, *48*, 620–624. [CrossRef]
21. Gasparrini, C. *Gold and Other Precious Metals from Ore to Market*; Springer: Berlin, Germany, 1993; 336p.
22. Kesler, S.E.; Chryssoulis, S.L.; Simon, G. Gold in porphyry copper deposits: Its abundance and fate. *Ore Geol. Rev.* **2002**, *21*, 103. [CrossRef]
23. Pals, D.W.; Spry, P.G. Telluride mineralogy of the low-sulfidation epithermal Emperor gold deposit, Vatukoula, Fiji. *Mineral. Petrol.* **2003**, *79*, 285–307. [CrossRef]
24. Plotinskaya, O.Y.; Kovalenker, V.A.; Seltmann, R.; Stanley, C.J. Te and Se mineralogy of the high-sulfidation Kochbulak and-Kairagach epithermal gold telluride deposits (Kurama Ridge, Middle Tien Shan, Uzbekistan). *Mineral. Petrol.* **2006**, *87*, 187–2006. [CrossRef]
25. Mavrogenes, J.; Henley, R.W.; Reyes, A.G.; Berger, B. Sulfosalt melts: Evidence of high-temperature vapor transport of metals in the formation of high-sulfidation lode gold deposits. *Econ. Geol.* **2010**, *105*, 257–262. [CrossRef]
26. Tolstykh, N.D.; Vymazalova, A.; Tuhy, M.; Shapovalova, M. Conditions of formation of Au-Se-Te mineralization in the Gaching.ore occurrence (Maletoyvayam ore field), Kamchatka, Russia. *Mineral. Mag.* **2018**, *82*, 649–674. [CrossRef]
27. Palyanova, G.A. Gold and silver minerals in sulfide ore. *Geol. Ore Depos.* **2020**, *62*, 383–406. [CrossRef]
28. Park, J.-W.; Campbell, I.H.; Kim, J.; Moon, J.-W. The role of late sulfide saturation in the formation of a Cu- and Au-rich magma: Insights from the platinum group element geochemistry of Niuatahi-Motutahi lavas, Tonga rear arc. *J. Petrol.* **2015**, *56*, 59–81. [CrossRef]
29. Li, Y.; Feng, L.; Kiseeva, E.S.; Gao, Z.; Du, Z.; Wang, F.; Shi, L. An essential role for sulfur in sulfide-silicate melt partitioning of gold and magmatic gold transport at subduction settings. *Earth Planet. Sci. Lett.* **2019**, *528*, 115850. [CrossRef]
30. Snoke, A.W.; Quick, J.E.; Bowman, H.R. Bear Mountain igneous complex, Klamath Mountains, California: An ultrabasic to silicic calc-alkaline suite. *J. Petrol.* **1981**, *22*, 501–552. [CrossRef]
31. Burns, L.E. The Border Ranges ultramafic and mafic complex, southcentral Alaska: Cumulate fractionates of island-arc volcanics. *Can. J. Earth Sci.* **1985**, *22*, 1020–1038. [CrossRef]
32. Kepezhinskas, P.K.; Reuber, I.; Tanaka, H.; Miyashita, S. Zoned calc-alkaline plutons in Northeastern Kamchatka, Russia: Implications for the crustal growth in magmatic arcs. *Mineral. Petrol.* **1993**, *49*, 147–174. [CrossRef]
33. Candela, P.A. A review of shallow, ore-related granites: Textures, volatiles, and ore metals. *J. Petrol.* **1997**, *38*, 1619–1633. [CrossRef]

34. Olson, N.H.; Dilles, J.H.; Kent, A.J.R.; Lang, J.R. Geochemistry of the Cretaceous Kaskanak Batholith and genesis of the Pebble porphyry Cu-Au-Mo deposit, Southwest Alaska. *Amer. Mineral.* **2017**, *102*, 1597–1621. [CrossRef]
35. Audetat, A. The metal content of magmatic-hydrothermal fluids and its relationship to mineralization potential. *Econ. Geol.* **2019**, *114*, 1033–1056. [CrossRef]
36. Kepezhinskas, P.K.; Kepezhinskas, N.P.; Berdnikov, N.V.; Krutikova, V.O. Native metals and intermetallic compounds in subduction-related ultramafic rocks from the Stanovoy mobile belt (Russian Far East): Implications for redox heterogeneity in subduction zones. *Ore Geol. Rev.* **2020**, *127*, 103800. [CrossRef]
37. Muntean, J.L.; Einaudi, M.T. Porphyry gold deposits of the Refugio district, Maricunga Belt, Northern Chile. *Econ. Geol.* **2000**, *95*, 1445–1472. [CrossRef]
38. Arif, J.; Baker, T. Gold paragenesis and chemistry at Batu Hijau, Indonesia: Implications for gold-rich porphyry copper deposits. *Mineral. Depos.* **2004**, *39*, 523–535. [CrossRef]
39. Crespo, J.; Reich, M.; Barra, F.; Verdugo, J.J.; Martinez, C. Critical metal particles in copper sulfides from the supergiant Rio Blanco porphyry Cu-Mo deposit, Chile. *Minerals* **2018**, *8*, 519. [CrossRef]
40. Chudnenko, K.V.; Palyanova, G.A. Thermodynamic properties of solid solutions in the Ag-Au-Cu system. *Russ. Geol. Geophys.* **2014**, *55*, 349–360. [CrossRef]
41. Palyanova, G.; Karmanov, N.; Savva, N. Sulfidation of native gold. *Amer. Mineral.* **2014**, *99*, 1095–1103. [CrossRef]
42. Palyanova, G.A.; Savva, N.E.; Zhuravkova, T.V.; Kolova, E.E. Gold and silver minerals in low-sulfidation ores of the Julietta deposit (northeastern Russia). *Russ. Geol. Geophys.* **2016**, *57*, 1171–1190. [CrossRef]
43. Kepezhinskas, K.B. Structural-metamorphic evolution of late Proterozoic ophiolites and Precambrian basement in the Central Asian foldbelt of Mongolia. *Precambrian Res.* **1986**, *33*, 209–223. [CrossRef]
44. Kepezhinskas, P.K.; Kepezhinskas, K.B.; Puchtel, I.S. Lower Paleozoic oceanic crust in Mongolian Caledonides: Sm-Nd and trace element data. *Geophys. Res. Lett.* **1991**, *18*, 1301–1304. [CrossRef]
45. Jahn, B.M. The Central Asian Orogenic Belt and growth of the continental crust in the Phanerozoic. *Geol. Soc. Lond. Spec. Publ.* **2004**, *226*, 73–100. [CrossRef]
46. Windley, B.F.; Alexeiev, D.; Xiao, W.; Kröner, A.; Badarch, G. Tectonic models for accretion of the Central Asian Orogenic Belt. *J. Geol. Soc. Lond.* **2007**, *164*, 31–47. [CrossRef]
47. Velikoslavinsky, S.D.; Kotov, A.B.; Kovach, V.P.; Tolmacheva, E.V.; Sorokin, A.A.; Sal'nikova, E.B.; Larin, A.M.; Zagornaya, N.Y.; Wang, K.L.; Chung, S.-L. Age and tectonic position of the Stanovoi metamorphic complex in the eastern part of the Central Asian foldbelt. *Geotectonics* **2017**, *51*, 341–352. [CrossRef]
48. Velikoslavinsky, S.D.; Kotov, A.B.; Salnikova, E.B.; Sorokin, A.A.; Larin, A.M.; Yakovleva, S.Z.; Kovach, V.P.; Tolmacheva, E.V.; Anisimova, I.V.; Plotkina, Y.V. Metabasalts of the Bryanta sequence of the Stanovoi complex of the Dzhugdzhur-Stanovoi superterrane, Central Asian fold belt: Age and geodynamic environment of formation. *Petrology* **2012**, *20*, 240–254. [CrossRef]
49. Jin, X.; Zhu, H. Determination of platinum-group elements and gold in geological samples with ICP-MS using sodium peroxide fusion and tellurium co-precipitation. *J. Anal. Atom. Spectrom.* **2000**, *15*, 747–751. [CrossRef]
50. Kepezhinskas, P.; Berdnikov, N.; Kepezhinskas, N.; Konovalova, N. Metals in Avachinsky peridotite xenoliths with implications for redox heterogeneity and metal enrichment in the Kamchatka mantle wedge. *Lithos* **2022**, *127*, 103800. [CrossRef]
51. Woodhead, J.; Eggins, S.; Gamble, J. High field strength and transition element systematics in island arc and back-arc basin basalts: Evidence for multi-phase melt extraction and a depleted mantle wedge. *Earth Planet. Sci. Lett.* **1993**, *114*, 491–504. [CrossRef]
52. Kepezhinskas, P.; McDermott, F.; Defant, M.; Hochstaedter, A.; Drummond, M.S.; Hawkesworth, C.J.; Koloskov, A.; Maury, R.C.; Bellon, H. Trace element and Sr-Nd-Pb isotopic constraints on a three-component model of Kamchatka arc petrogenesis. *Geochim. Cosmochim. Acta* **1997**, *61*, 577–600. [CrossRef]
53. Drummond, M.S.; Defant, M.J.; Kepezhinskas, P. The petrogenesis of slab derived trondhjemite-tonalite-dacite/adakite magmas. *Trans. R. Soc. Edinb. Earth Sci.* **1996**, *87*, 205–216.
54. Kepezhinskas, P.; Berdnikov, N.; Kepezhinskas, N.; Konovalova, N. Adakites, high-Nb basalts and copper-gold deposits in magmatic arcs and collisional orogens: An overview. *Geosciences* **2022**, *12*, 29. [CrossRef]
55. Kepezhinskas, P.K.; Defant, M.J.; Drummond, M.S. Progressive enrichment of island arc mantle by melt-peridotite interaction inferred from Kamchatka xenoliths. *Geochim. Cosmochim. Acta* **1996**, *60*, 1217–1229. [CrossRef]
56. Kepezhinskas, N.; Kamenov, G.D.; Foster, D.A.; Kepezhinskas, P. Petrology and geochemistry of alkaline basalts and gabbroic xenoliths from Utila Island (Bay Islands, Honduras): Insights into back-arc processes in the Central American volcanic arc. *Lithos* **2020**, *352–353*, 105306. [CrossRef]
57. Beard, J.S. Characteristic mineralogy of arc-related cumulate gabbros: Implications for the tectonic setting of gabbroic plutons and for andesite genesis. *Geology* **1986**, *14*, 848–851. [CrossRef]
58. Sun, S.-S.; McDonough, W.F. Chemical and isotopic systematics of oceanic basalts: Implications for mantle composition and processes. *Geol. Soc. Lond. Spec. Publ.* **1989**, *42*, 313–345. [CrossRef]
59. Vincent, E.A.; Crocket, J.H. Studies in the geochemistry of some basic and ultrabasic rocks and some meteorites. *Geochim. Cosmochim. Acta* **1960**, *18*, 143–148. [CrossRef]
60. Oshin, I.O.; Crocket, J.H. Noble metals in Thetford Mines Ophiolite, Quebec, Canada. Part I: Distribution of gold, iridium, platinum and palladium in the ultramafic and gabbroic rocks. *Econ. Geol.* **1982**, *77*, 1556–1570. [CrossRef]

61. Turekian, K.K.; Wedepohl, K.H. Distributions of the elements in some units of the Earth's crust. *Geol. Soc. Amer. Bull.* **1961**, *72*, 175–192. [CrossRef]
62. Chou, C.L.; Shaw, D.M.; Crocket, J.H. Siderophile trace elements in the earth's oceanic crust and upper mantle. *J. Geophys. Res.* **1983**, *88*, A517–A518. [CrossRef]
63. Wedepohl, K.H. The composition of the continental crust. *Geochim. Cosmochim. Acta* **1995**, *59*, 1217–1232. [CrossRef]
64. Wise, J. *Gold Recovery, Properties and Applications*; D. Van Nostrand Company: Taylorville, IL, USA, 1964; 167p.
65. Berdnikov, N.; Nevstruev, V.; Kepezhinskas, P.; Astapov, I.; Konovalova, N. Gold in mineralized volcanic systems from theLesser Khingan Range (Russian Far East): Textural types, composition and possible origins. *Geosciences* **2021**, *11*, 103. [CrossRef]
66. Raub, E.Z. Die Legierungen des Goldes mit Chrom, Molybdan und Wolfram. *Int. J. Mater. Res.* **1960**, *51*, 290–291. [CrossRef]
67. Lyakishev, N.P. *Phase Diagrams for Binary Metallic Systems*; Mashinostroenie: Moscow, Russia, 1997; 1024p. (In Russian)
68. Petrunin, I.E.; Grzhimal'skii, L.L. Interaction of tungsten with copper, manganese, silver, and tin. *Metal Sci. Heat Treat.* **1969**, *11*, 24–26. [CrossRef]
69. Kelley, K.A.; Cottrell, E. Water and the oxidation state of subduction zone magmas. *Science* **2009**, *325*, 605–607. [CrossRef] [PubMed]
70. Humphreys, M.C.S.; Brooker, R.A.; Fraser, D.G.; Burgisser, A.; Mangan, M.T.; McCammon, C. Coupled interactions between volatile activity and Fe oxidation state during arc crustal processes. *J. Petrol.* **2015**, *56*, 795–814. [CrossRef]
71. Lazar, C. Using silica activity to model redox-dependent fluid compositions in serpentinites from 100 to 700 °C and from 1 to 20 kbar. *J. Petrol.* **2020**, *61*, egaa101. [CrossRef]
72. Evans, K.A.; Frost, B.R. Deserpentinization in subduction zones as a source of oxidation in arcs: A reality check. *J. Petrol.* **2021**, *62*, egab016. [CrossRef]
73. Tang, M.; Erdman, M.; Eldridge, G.; Lee, C.-T.A. The redox "filter" beneath magmatic orogens and the formation of continental crust. *Sci. Adv.* **2018**, *4*, eaar4444. [CrossRef] [PubMed]
74. Tollan, P.; Hermann, J. Arc magmas oxidized by water dissociation and hydrogen incorporation in orthopyroxene. *Nat. Geosci.* **2019**, *12*, 667–671. [CrossRef]
75. Berdnikov, N.V.; Nevstruev, V.G.; Kepezhinskas, P.K.; Krutikova, V.O.; Konovalova, N.S.; Astapov, I.A. Silicate, Fe-oxide, and Au-Cu-Ag micropsherules in ores and pyroclastic rocks of the Kostenga iron deposit, in the Far East of Russia. *J. Russ. Pac. Geol.* **2021**, *15*, 236–251. [CrossRef]
76. Rapson, W.S. The metallurgy of the coloured carat gold alloys. *Gold Bull.* **1990**, *23*, 125–133. [CrossRef]
77. Townley, B.K.; Herail, G.; Maksaev, V.; Palacios, C.; de Parseval, P.; Sepuldeva, F.; Orellana, R.; Rivas, P.; Ulloa, C. Gold grain morphology and composition as an exploration tool: Application to gold exploration in covered areas. *Geochem. Explor. Env. Anal.* **2003**, *3*, 29–38. [CrossRef]
78. Chapman, R.J.; Mortensen, J.K.; Crawford, E.; LeBarge, W. Microchemical studies of placer and lode gold in Bonanza and Eldorado creeks, Klondike District, Yukon, Canada: Evidence for a small, gold-rich, orogenic hydrothermal system. *Econ. Geol.* **2010**, *105*, 1393–1410. [CrossRef]
79. Chapman, R.J.; Mortensen, J.K.; LeBarge, W.P. Styles of lode gold mineralization contributing to the placers of the Indian River and Black Hills Creek, Yukon Territory, Canada as deduced from microchemical characterization of placer gold grains. *Miner. Depos.* **2011**, *46*, 881–903. [CrossRef]
80. Oen, I.; Kieft, C. Nickeline with pyrrhotite and cubanite exsolutions, Ni-Co-rich loellingite and an Au-Cu-alloy in Cr-Ni-ores from Beni-Bousera, Morocco. *Neues Jahrb. Miner. Monatsh.* **1974**, *115*, 1–8.
81. Kepezhinskas, P.; Defant, M.J.; Widom, E. Abundance and distribution of PGE and Au in the island-arc mantle: Implications for sub-arc metasomatism. *Lithos* **2002**, *60*, 113–128. [CrossRef]
82. Widom, E.; Kepezhinskas, P.; Defant, M. The nature of metasomatism in the sub-arc mantle wedge: Evidence from Re-Os isotopes in Kamchatka peridotite xenoliths. *Chem. Geol.* **2003**, *196*, 283–306. [CrossRef]
83. Saunders, J.E.; Pearson, N.J.; O'Reilly, S.Y.; Griffin, W.L. Gold in the mantle: A global assessment of abundance and redistribution processes. *Lithos* **2018**, *322*, 376–391. [CrossRef]
84. Anoshin, G.N.; Kepezhinskas, V.V. Petrochemical features related to gold distribution for the Cenozoic volcanic rocks of the Kuril-Kamchatka province. *Geochem. Int.* **1972**, *9*, 618–629.
85. Kutyrev, A.; Zelenski, M.; Nekrylov, N.; Savelyev, D.; Kontonikas-Charos, A.; Kamenetsky, V.S. Noble metals in arc basaltic magmas worldwide: A case study of modern and pre-historic lavas of the Tolbachik volcano, Kamchatka. *Front. Earth Sci.* **2021**, *9*, 791465. [CrossRef]
86. Pitcairn, I.K.; Craw, D.; Teagle, D.A.H. Metabasalts as sources of metals in orogenic gold deposits. *Mineral. Depos.* **2014**, *50*, 373–390. [CrossRef]
87. Tomkins, A.G.; Rebryna, K.C.; Weinberg, R.F.; Schaefer, B.F. Magmatic sulfide formation by reduction of oxidized arc basalt. *J. Petrol.* **2012**, *53*, 1537–1567. [CrossRef]
88. Botcharnikov, R.; Linnen, R.; Wilke, M.; Holtz, F.; Jugo, P.; Berndt, J. High gold concentrations in sulphide-bearing magma under oxidizing conditions. *Nat. Geosci.* **2011**, *4*. [CrossRef]
89. Luhr, J.F. Experimental phase relations of water- and sulfur-saturated arc magmas and the 1982 eruptions of El Chichón volcano. *J. Petrol.* **1990**, *31*, 1071–1114. [CrossRef]

90. Baker, L.L.; Rutherford, M.J. Crystallization of anhydrite-bearing magmas. *Earth Environ. Sci. Trans. R. Soc. Edinb.* **1996**, *87*, 243–250. [CrossRef]
91. Richards, J.P. Porphyry copper deposit formation in arcs: What are the odds? *Geosphere* **2021**. [CrossRef]
92. Matjuschkin, V.; Blundy, J.D.; Brooker, R.A. The effect of pressure on sulphur speciation in mid- to deep-crustal arc magmas and implications for the formation of porphyry copper deposits. *Contrib. Mineral. Petrol.* **2016**, *171*. [CrossRef]